The Astrophysical Journal, 744:8 (12pp), 2012 January 1 doi:10.1088/0004-637X/744/1/8
© 2012. The American Astronomical Society. All rights reserved. Printed in the U.S.A.

CHARGING AND COAGULATION OF DUST IN PROTOPLANETARY PLASMA ENVIRONMENTS

L. S. Matthews, V. Land, and T. W. Hyde
Center for Astrophysics, Space Physics, and Engineering Research, Baylor University, Waco, TX 76798-7316, USA; lorin_matthews@baylor.edu
Received 2011 April 5; accepted 2011 September 13; published 2011 December 7

ABSTRACT

Combining a particle–particle, particle–cluster, and cluster–cluster agglomeration model with an aggregate charging model, the coagulation and charging of dust particles in plasma environments relevant for protoplanetary disks have been investigated, including the effect of electron depletion in high dust density environments. The results show that charged aggregates tend to grow by adding small particles and clusters to larger particles and clusters, and that cluster–cluster aggregation is significantly more effective than particle–cluster aggregation. Comparisons of the grain structure show that with increasing aggregate charge the compactness factor, ϕ_σ, decreases and has a narrower distribution, indicating a fluffier structure. Neutral aggregates are more compact, with larger ϕ_σ, and exhibit a larger variation in fluffiness. Overall, increased aggregate charge leads to larger, fluffier, and more massive aggregates.

Key words: accretion, accretion disks – planets and satellites: formation – plasmas – protoplanetary disks

Online-only material: color figures

1. THE FORMATION OF PLANETS

At the time of writing more than 500 exoplanets have been observed with more than 400 of these confirmed, and more planets are being detected and confirmed on a weekly basis.[1] Even though these discoveries show that the process of planet formation is in itself a general one, they have also shown that our solar system is everything but the perfect example of the average planetary system, Pluto, or no Pluto. Partly due to the inherent bias of the available observational techniques, many of the earliest discovered systems involved large gaseous planets orbiting close to the parent star and planets on very eccentric orbits, much in contrast with our solar system (Ollivier et al. 2009). Since many early planet formation theories were based on the solar system (and in many cases these were then tested against our solar system), these observations make clear that our knowledge of planet formation is incomplete.

The environment in which planet formation takes place is generally accepted to be a protoplanetary disk (PPD), a disk of gas and small (nanometer to millimeter sized) dust particulates accreting matter onto the central young stellar object (YSO), a famous example of which is observed around β-pictoris (Smith & Terrile 1984). There are many different models for the formation of gaseous and rocky planets in such disks: the *core-accretion* model (Pollack 1984), accompanied by *planet migration* theories (Raymond et al. 2006), or *disk-instability* models (Boss 1997). All of these involve an early stage in which the dust particles collide and stick together to form the initial seeds for planetesimal formation. This earliest stage is the topic of this paper, a stage which sets the starting point and initial conditions for the various planet formation theories and models currently under debate.

One of the oldest problems in accretion disk studies is the apparent inability of the gas (due to the minute viscosity of the gas) to transfer angular momentum outward, while transferring mass inward. A possible solution to this problem was presented in the α*-model*, in which turbulent viscosity provides sufficient friction for momentum transfer (Shakura & Sunyaev 1973). However, no specific mechanism providing the turbulence was presented; the presence thereof was simply assumed.

Two decades later, a connection was made between a magnetic instability in Couette flows, called the magnetorotational instability (MRI; Velikhov 1959), and the turbulence arising in accretion disks. This has become the most popular theory for the description of turbulence in accretion disks (Balbus & Hawley 1991). With this theory, however, arises one of the current dichotomies in studies of the microphysics of the early stages of planet formation.

The MRI present in accretion disks *requires* the presence of an (albeit weakly) ionized medium, since the magnetic field involved has to be (albeit weakly) coupled to the disk matter. On the other hand, almost all studies to date involving the collision and subsequent sticking of microparticles have considered only neutral particulates in a gaseous environment. This is true for both theoretical and numerical studies (Kempf et al. 1999; Dominik & Tielens 1997; Zsom et al. 2011), as well as experimental studies (Blum et al. 2000), although a few experiments examining magnetic grains have been performed (Nübold et al. 2002). Charging effects are usually considered to be insignificant or are merely mentioned as an afterthought (Blum & Wurm 2008).

A few recent exceptions include the experimental observation of particle coagulation under microgravity conditions due to triboelectric charging (Konopka et al. 2005), in which the authors concluded that the formation of aggregates occurred on very short timescales, even more rapidly than could be explained simply by charge-enhanced collision cross sections. Similarly, numerical simulations using binary particle–particle, particle–cluster, and cluster–cluster collisions showed how charged aggregates coagulated rapidly due to electric multipole interactions, originating from the fluffy structure of the charged aggregates (Matthews et al. 2007), even when the total charge on the aggregates is very small.

Simulations where the charging due to the collection of charged particles from a plasma environment were taken into account include Okuzumi (2009) and Matthews & Hyde (2009), using different models, such as Monte Carlo and *N*-body models, and computations based on the Smoluchowski equation. More recently, the importance of aggregate–plasma interactions was explicitly considered by investigating how the depletion of free electrons in the plasma through absorption on the aggregates can

[1] http://www.exoplanets.org, http://www.exoplanet.eu

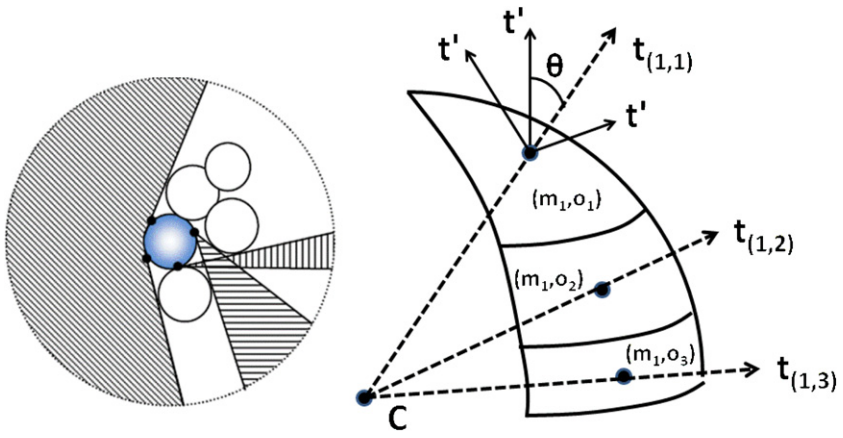

Figure 1. Two-dimensional representation of the OML_LOS geometry, as shown on the left. Different points on a monomer in an aggregate are partly shadowed from the outside plasma by other monomers. The dashed areas indicate the open, unblocked lines of sight for four points on a monomer. These unblocked lines of sight are used to approximate the solid angle in the integral for the current density. An illustration of the test directions defined in the model to calculate the current density to a surface patch on one of the monomers is shown on the right. C indicates the center of the monomer with three surface patches having coordinates (m_1, o_1), (m_1, o_2), (m_1, o_3) shown. The vectors t, which are also the normal vectors to the surface patches, show some of the test-directions for determination of the open lines of sight. The vectors t' indicate such directions applied on one of the patches. When one of these vectors intersects another monomer in the aggregate, or points inward into the monomer the patch sits on, a 0 is assigned to that direction, otherwise a 1. Only surface patches with at least one open line of sight contribute to the integral. $\cos(\theta)$ is calculated for all test-directions to provide the components normal to the surface patch.

(A color version of this figure is available in the online journal.)

introduce an electrostatic barrier against aggregate formation (Okuzumi et al. 2011a, 2011b).

In this paper we present a numerical study of the coagulation and charging of dust particles and aggregates in different plasma environments relevant to PPDs, including the effect of free electron depletion due to absorption on the dust. The collision statistics are studied and it is shown that for the initial formation of small aggregates, increased charge reduces the collision probability. It is furthermore shown that charged aggregates preferably incorporate the largest monomers from the initial monomer size-distribution, while the distribution of included monomers incorporated in neutral aggregates very closely follows the initial monomer size-distribution. This results in larger, more massive, and more porous aggregates for highly charged aggregates, while neutral coagulation results in the smallest, lightest, and most compact aggregates.

2. CHARGING AND COLLISIONS OF AGGREGATES

The results in this study were obtained using a Particle–Particle/Particle–Cluster/Cluster–Cluster Agglomeration (PPA/PCA/CCA) model, Aggregate_Builder, coupled to an aggregate charging code, Orbital Motion Limited Line of Sight (OML_LOS). This section will briefly explain OML theory, as well as the LOS approximation used to calculate the charge on the aggregates. Next, the principles of Aggregate _Builder will be discussed. Since the fluffiness of particles is an important property, we will also briefly explain two ways of defining fluffiness, or porosity, namely through the *fractal dimension* and the *compactness factor*.

2.1. OML Theory and Line of Sight Approximation

There are many mechanisms that result in the charging of dust in a plasma environment, including photodetachment (for instance by UV radiation), secondary electron emission (through the impact of energetic electrons), radioactive charging, triboelectric charging, and more (Mendis & Rosenberg 1994). However, in this study, we limit ourselves to charging through the collection of charged particles from the surrounding plasma.

The charging of a single particle immersed in plasma is described by OML theory, originally derived for Langmuir probe measurements (Allen 1992). The current density due to incoming particle species α (here we assume $\alpha = e$ or $\alpha = i$ for electrons and ions carrying one positive electron charge, respectively) to a point on the surface of a particle is given by

$$J_\alpha(t) = n_\alpha q_\alpha \iiint f_\alpha(v_\alpha) v_\alpha \cos(\theta) d^3\overrightarrow{v_\alpha}, \quad (1)$$

with n_α the plasma density very far from the particle, q_α the charge of the incoming plasma particle, $f_\alpha(v_\alpha)$ the velocity distribution function of the plasma particles and $v_\alpha \cos(\theta)$ the velocity component of the incoming plasma particle perpendicular to the surface. By using $d^3\overrightarrow{v_\alpha} = v_\alpha^2 dv_\alpha d\Omega$, with $d\Omega$ the solid angle, we can split the integral to obtain

$$J_\alpha(t) = n_\alpha q_\alpha \int_{v_m(t)}^{\infty} f_\alpha(v_\alpha) v_\alpha^3 dv_\alpha \times \iint \cos(\theta) d\Omega. \quad (2)$$

Here, $v_m(t) = \sqrt{2q_\alpha V_D(t)/m_\alpha}$ is the minimum velocity a plasma particle with the same polarity of charge as the dust particle must have to reach the dust particle surface. V_D is the dust particle surface potential. For plasma particles with the opposite polarity of charge, $v_m = 0$.

For a single spherical particle the integral over the solid angle is trivial, but for an aggregate the integral becomes complicated, since one monomer in the aggregate can block part of the solid angle available to a point on another monomer in the aggregate, as illustrated in Figure 1, on the left. As an example of this, the *open* solid angle (in this two-dimensional representation) for four points on one of the monomers in a small aggregate is indicated by the dashed areas.

In order to calculate the current density of species α to a monomer in the aggregate at a given time, the expression in Equation (2) is split into two parts,

$$J_\alpha(t) = J_\alpha(v_\alpha, t) \times \text{LOS_factor}. \quad (3)$$

$J_\alpha(v_\alpha, t)$ is the component of the current density which only depends on the speed of the plasma particles approaching the

aggregates, whereas LOS_factor is the numerical approximation to the solid-angle integral, which depends on the open lines of sight.

In order to obtain LOS_factor, the surface of the monomer is divided into patches with coordinates (m, o), similar to the longitude–latitude system, but with each surface patch having the same area, A. Vectors pointing from the center of the monomer to these surface points define $[m \times o]$ test directions, $\overrightarrow{t}$. Using these directions for each surface point defines the test lines of sight, $\overrightarrow{t}'$. These lines of sight are determined to be *blocked* if they intersect any other monomer in the aggregate, or the monomer the surface points reside on, and *open* otherwise. Each separate line of sight is then assigned a value of LOS$(t') =$ 0, or 1, respectively. At the same time, the cosines of the angles between the normal direction of the patch and each LOS is determined; $\cos(\theta = \angle(\overrightarrow{t}, \overrightarrow{t}'))$. Figure 1 illustrates this method, on the right. The line of sight factor for the patch at point (m, o), LOS_factor$(m, o) = \sum$LOS$(t') \times \cos\theta \times \Delta\Omega$, where $\Delta\Omega$ is the fractional solid angle extended about any test direction; $\Delta\Omega = 4\pi/(m \times o)$, and the sum is over all test lines of sight, $\overrightarrow{t}'$.

The net current of species α to a patch at point (m, o) at a given time, $I_{\alpha,(m,o)}(t)$, can now be found by multiplying the current density by the area of the patch: $I_{\alpha,(m,o)}(t) = J_{\alpha,(m,o)}(v_\alpha, t) \times A \times$LOS_factor$(m, o)$. Summing over the species α provides the change in the surface charge on the patch during a time interval dt, $dQ_{D,(m,o)}(t) = \Sigma_\alpha I_{\alpha,(m,o)}(t)dt$. Note that the current to the patch depends on $v_m(t)$, which in turn depends on $V_{D,(m,o)}(t)$ (hence on $Q_{D,(m,o)}(t)$), so that the solution requires numerical iteration until equilibrium is reached. The change in charge of the whole monomer is then obtained by adding up the contribution of all the patches. The change in charge of the whole aggregate is obtained by adding the contributions from each of the N monomers. This process is iterated in time until the change in aggregate charge becomes negligible, $dQ_{\rm agg} < 0.0001\%$, at which point on average the net current to the whole aggregate will be zero.

For sufficient resolution, we use over 400 patches per monomer ($m \times o = 20 \times 21$). The largest aggregates in this study contain just over 2000 monomers. Since each time iteration requires on the order of 100 time steps, the total charge calculation for the largest aggregates require on the order of 10^8 iterations. Obviously, the computations for determining the detailed charge structure are very time consuming.

The dipole moment for the aggregate is found in a similar manner. The contribution of each patch is computed and then summed to obtain the dipole moment on each monomer. To obtain the dipole moment of the aggregate as a whole, the contribution of each monomer is then added up. The monopole and dipole charges are then used in the calculations of the collisions performed in Aggregate_Builder, as discussed below.

In reality, charged particles (electrons and ions) approaching the charged aggregate will not travel exactly along straight lines but will follow curved trajectories in the potential around the aggregate. As a simple check, we computed the surface potential on a single, isolated spherical dust particle in an equal density hydrogen-electron plasma in thermal equilibrium, and compared it with the classical *Spitzer* result (the particle potential becomes $V_D \approx -2.51 k_B T/e$ (T in K)) (Spitzer 1941). For a one micron diameter dust particle, the difference between the OML results and our numerical OML_LOS result was less than 0.26%, showing that the OML_LOS approximation works very well.

2.2. The Plasma Environment

In a standard PPD model for the early solar system, the fractional ionization according to recent chemistry models is found to vary between $10^{-13} < \xi_e \leqslant 10^{-3}$ (Semenov et al. 2004). Even though this is sufficient to cause significant charging of the dust, the majority of collisions for charged plasma particles will occur with neutral gas particles, rather than with other charged plasma particles, or the dust. The mean free path for the plasma particles can then be approximated by $l \sim (n\sigma)^{-1}$.

In this paper, we focus on one location in the PPD, namely at 1 AU from the central YSO and at $z = 0.5H$, where H is the vertical scale height, defined by $H = c_g/\Omega_k$, with c_g and Ω_k the local sound speed and Kepler rotation frequency, respectively. In the mid-plane, a distance of 1 AU from the central YSO, the gas density is estimated at $n \sim 10^{20}$ m^{-3} (Willacy et al. 1998). Since $n(z) \propto \exp(-z^2/2H^2)$, the density at $z = 0.5H$ will therefore roughly be $n = 8.8 \times 10^{19}$ m^{-3}. The collision cross section can be approximated by $\sigma = \pi d^2$, where d is the classical diameter of the gas particles. Setting the classical radius of the hydrogen molecule (the assumed dominant species) equal to twice the Bohr radius, we approximate d by $d \approx 4a_0 = 2.12 \times 10^{-10}$ m, so that $\sigma \approx 1.41 \times 10^{-19}$ m^2, which makes the mean free path approximately 8 cm. This is much smaller than the length scales relevant for dust coagulation, therefore the electrons and ions can be assumed to be collisional within the PPD.

For neutral gas, the OML_LOS routine is not used and the charge on the aggregates is set to 0 and remains that way. Due to the large collisionality of the plasma species, we assume thermal equilibrium holds, so that the Maxwellian distribution is used for the plasma species:

$$f_\alpha(v_\alpha) = \left(\frac{m_\alpha}{2\pi k_B T}\right)^{3/2} \exp\left(-\frac{m_\alpha v_\alpha^2}{2k_B T} - \frac{q_\alpha V_D}{k_B T}\right), \quad (4)$$

with V_D the dust particle surface potential and m_α and T the electron/ion mass and the gas temperature, respectively.

In equilibrium, the current densities of ions and electrons balance, and the equilibrium dust surface potential (and charge) is reached. Local quasi-neutrality of the plasma including the dust charge density contribution reads

$$-en_e - eZ_D n_D + en_i = 0, \quad (5)$$

where we have assumed one single ion species to provide the dominant positive charging current, and Z_D is the dust charge number. This equation can be rewritten as

$$n_i = n_e(1 + P), \quad (6)$$

with $P = n_D z_D/n_e$ the Havnes parameter, which shows the ratio of negative charge bound on the dust to the negative charge moving freely in the plasma (Whipple et al. 1985). Due to the electron depletion, the ratio of free electrons to free ions is reduced, leading to a net reduction of the dust charge. We consider three cases: $n_e/n_i = (1 + P)^{-1} = 0.1$, 0.5 and 1, so that in total we consider four plasma environments when we include the neutral coagulation.

2.3. Aggregate_Builder

Aggregate_Builder is based on an N-body code originally developed to investigate the gravitational interactions between planetesimals and objects in rocky rings (Richardson 1993). The

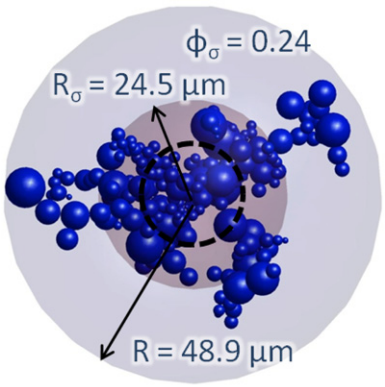

Figure 2. Illustration of the compactness factor and equivalent radius for one aggregate. The lighter colored circle indicates the maximum aggregate radius, R, defined as the maximum extent of the aggregate from the COM, which for a single monomer would equal the monomer radius, a. The darker inner circle indicates the orientation-averaged equivalent radius R_σ, as defined in the text. For this aggregate the compactness factor, ϕ_σ, is calculated as 0.24. This means that the total volume of all the monomers fills a smaller equivalent sphere of radius 0.68 R_σ, as indicated by the black dashed circle.

(A color version of this figure is available in the online journal.)

code has since been modified and extended to include the effects of charged particles and magnetic fields (Matthews & Hyde 2003; Vasut & Hyde 2001; Qiao et al. 2007). The modified code treats accelerations caused by interactions of charged grains as well as rotations induced by torques due to the charge or magnetic dipole moments (Matthews et al. 2007; Perry et al. 2010). These dipole–dipole interactions have been shown to greatly enhance the collision rate, even for like-charged particles (Matthews & Hyde 2009).

Aggregate_Builder is used to study pairwise interactions of colliding particles in the center of mass (COM)-frame of the target particle. The incoming particle has a velocity directed toward the target particle to within an offset-distance $(R_{\sigma,t} + R_{\sigma,i})/2$ of the COM, where $R_{\sigma,t}$ and $R_{\sigma,i}$ are the orientation-averaged equivalent radii of the target and incoming particles, respectively, as indicated in Figure 2 and described in Section 2.5. Libraries of aggregates are created from successful collisions, which can then be used as starting points in N-body codes. This allows modeling of the aggregation of large distributions of aggregates. Information on the missed collisions is saved for collision statistics.

Aggregates are built in three steps. First-generation aggregates are built by additions of single monomers, up to a size of $N = 20$. A charged monomer (with a charge determined by the plasma temperature and densities) is randomly chosen from a size distribution and placed at the origin. Another randomly selected monomer is "shot" toward the first monomer. The initial velocity is a combination of Brownian motion and the velocity derived from turbulence theory, and as discussed in Section 2.4, these velocities are shown to be low enough for grains to stick at the point of contact without fragmentation. The orientation and position of each particle is tracked and a collision is detected only when two monomers actually overlap. The new aggregate properties are then updated, including the charge (calculated with OML_LOS), and the resultant aggregate is saved to the first-generation aggregate library. The origin is then defined to be the COM of the new aggregate and the process is repeated. In total, 7000 aggregates were formed and stored in the first generation, for each plasma environment simulated.

The second generation is constructed by randomly selecting one of the aggregates from the first-generation library, containing aggregates with $2 \leqslant N \leqslant 20$ and placing it at the origin. In 60% of the cases a randomly selected monomer is shot toward the aggregate, while in 40% of the cases another aggregate randomly chosen from the library is used. Both the monopole and dipole interactions can induce torques on the aggregates, causing them to spin and their trajectories to deviate from straight lines. Figure 3 shows the importance of such dipole interactions. When dipole interactions are ignored in the calculations, the resulting aggregate has an entirely different geometry and fluffiness. Aggregates containing up to at least 200 monomers are constructed this way, charged in OML_LOS and stored in the library for second-generation aggregates. In total, 4000 aggregates were formed and stored in the second-generation libraries for each plasma environment.

Finally, the third generation is created by randomly selecting an aggregate from the second-generation library, containing aggregates with $3 \leqslant N \lesssim 200$, and placing it at the origin. In 50% of the cases the incoming particle is a monomer, in 30% of the cases an aggregate from the first-generation library and in the remaining 20% of the cases an aggregate from the second-generation library, resulting in the growth of aggregates with $N \approx 2000$. These aggregates are then charged in OML_LOS. In total, 1500 aggregates were formed and stored in the third-generation libraries for each plasma environment.

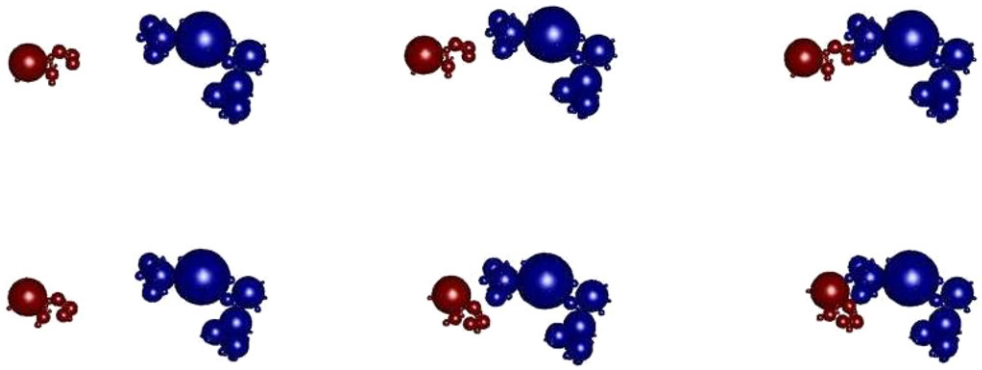

Figure 3. Example showing the importance of dipole interactions. The top row shows three snapshots of a collision between two charged aggregates when dipole interactions are ignored. The particles approach along a straight-line trajectory, as in a ballistic collision, with the particles slowing as they approach each other. The bottom row shows another collision between the same aggregates, but now the dipole interactions are taken into account. The rotation of the aggregates results in a completely different geometry of the final aggregate. In this case, the interaction time between the two aggregates is also longer due to the rotation changing the orientation of the aggregate.

(A color version of this figure is available in the online journal.)

2.4. Relative Particle Velocities in Turbulent Flows

Assuming a capacitor model for dust particles, the charge can be related to the surface potential by $Q_D = 4\pi\epsilon_0 V_D a$, with a the particle radius. For a Maxwellian hydrogen plasma this gives $Q_D \approx -10\pi\epsilon_0 k_B T a/e$, or in more useful units, $Q_D \approx -1700e \times T(\mathrm{eV}) \times a(\mu\mathrm{m})$. For two particles having radii a_1 and a_2 and charge Q_1 and Q_2 to collide and stick, they must have sufficient energy to overcome the repulsive Coulomb interaction between them. Their initial kinetic energy, $K = 0.5\mu v_r^2$, with $\mu = m_1 m_2/(m_1 + m_2)$ the reduced mass and v_r the relative particle velocity, should therefore be larger than $U = Q_1 Q_2/4\pi\epsilon_0\Delta$ with $\Delta = a_1 + a_2$. The minimum relative velocity is then given by $v_{r,\min} = \sqrt{2U/\mu}$.

As an example, the repulsive interaction energy between a $0.5\,\mu$m and a $10\,\mu$m silicate particle (with mass density $\rho = 2.5$ g cm^{-3}) in our simulation in a hot PPD environment with $T \approx 0.1$ eV, is given by $U = 85 * 1700e^2/4\pi\epsilon_0(10.5 \times 10^{-6}) \approx 20$ eV. This gives $v_{r,\min} \approx 7$ cm s^{-1}. Brownian motion results in a relative particle velocity of $v_{r,B} = \sqrt{8k_B T/\mu\pi} \approx 0.5$ cm s^{-1}, which is clearly not large enough to allow successful collisions between these charged particles. (Interestingly enough, the required velocity for two particles with $a = 0.5\,\mu$m is also 7 cm s^{-1}, which shows that Brownian motion is also unable to account for successful collisions between the smallest charged monomers in our distribution, with the smallest repulsive interaction energy.)

Even though there are different mechanisms that can provide additional velocities to a particle in a PPD, for example, radial drift and gravitational settling (Brauer et al. 2008), it has been shown that the corresponding velocities are relatively small. In Rice et al. (2004) the radial drift for micron-sized particles in a disk at 1 AU was found to be much less than 0.1 cm s^{-1}, while in Dullenmond & Dominik (2004) the gravitational settling time was found to be several orders of magnitude longer than the local Kepler time, corresponding to slow particle settling velocities. We therefore assume that in this case turbulence is the primary contributor to the relative velocities for dust particles in the PPD.

A complete derivation of the relative particle velocities in turbulent flow for different regimes is provided in Ormel & Cuzzi (2007). We here limit ourselves to the *small particle* regime, where dust is *strongly coupled* to the turbulent eddies. In this case, the relative velocity between two particles (indicated by subscripts 1 and 2) is given by

$$v_{\mathrm{turb}} = \sqrt{\frac{3}{2}} V_\eta \frac{(t_1 - t_2)}{t_\eta}, \tag{7}$$

with $t_s = 3m/4c_g\rho_g\sigma$ the stopping time of particle s, where c_g and ρ_g are the sound speed in the surrounding medium and the mass density of the surrounding medium, respectively, m is the dust particle mass and σ its geometric cross section (Weidenschilling 1984). V_η and t_η are the characteristic turnover velocity and time scale, respectively, which are related to the velocity and time scale of the largest eddies, on the Lagrangian scale, through the Reynolds number of the turbulent flow: $V_\eta \sim L_\eta/t_\eta$, $L_\eta = Re^{-3/4} L_L$ and $t_\eta = t_L Re^{-1/2}$.

For the definition of the large eddy length, time, and velocity scales, we follow Cuzzi et al. (2001) and adopt

$$V_L = \sqrt{\alpha} c_g, \tag{8}$$

$$L_L = \sqrt{\alpha} H, \tag{9}$$

$$t_L = \Omega_K^{-1}, \tag{10}$$

similar to the method used in Okuzumi et al. (2011b). With the above choice, the Reynolds number, defined as $Re = V_L L_L/\nu_m$, with ν_m the *molecular* viscosity of the gas in the disk, becomes $Re = \alpha c_g H/\nu_m$, which then corresponds to the *α-model* for the turbulent viscosity (Shakura & Sunyaev 1973), which, in simple terms, relates the turbulence in the disk to the thickness of the disk through the definition of the scale height.

2.5. Defining Fluffiness: Fractal Dimension and Compactness Factor

The fluffiness of an aggregate is very important to the coagulation process, since a fluffier aggregate couples more effectively to the gas in PPDs than a compact aggregate (Nakamura & Hidaka 1998). It also has different optical properties than a compact particle (Hage & Greenberg 1990), can provide a larger surface area for chemical reactions occurring in PPDs (Ehrenfreund 2003), and has a larger collisional cross section. In order to provide consistent statements about the fluffiness of the aggregates resulting from our simulations, we therefore need a consistent measurement, which is computationally robust and inexpensive at the same time.

One method commonly used is the fractal dimension. The method employed in our simulations is the Hausdorff dimension. In this method we place a box around the aggregate, with side X_0, so that the largest dimension of the aggregate just fits inside the box, and then divide this box into small sub-boxes with size $x \ll X_0$. We then count the number of sub-boxes, B, that are occupied by any part of the aggregate to obtain the fractal dimension as

$$d_F = \frac{\log B}{\log(X_0/x)}. \tag{11}$$

In the limit of a completely compact aggregate the above approaches three, and in the limit of a completely linear aggregate it approaches one. Although this represents a relatively simple method, the outcome depends strongly on the size of the sub-boxes used (hence the number of boxes to count) and becomes computationally rather expensive. Furthermore, the side length of the sub-boxes, x, should be at least as small as the diameter of the smallest monomer in the aggregate, which makes this method difficult to apply to polydisperse monomer distributions, such as those being considered in this study.

A more contemporary method is based on the idea of a compactness factor (Min et al. 2006). In this case, the aggregate is projected on a plane and the projected surface area A_i is calculated. The equivalent radius, R_i, is then defined by equating this area to the area of a circle, $A_i = \pi R_i^2$. Averaging this over many orientations yields an average equivalent radius, R_σ. The ratio of the total volume of all the monomers to the volume of the equivalent sphere with radius R_σ then defines the compactness factor

$$\phi_\sigma = \frac{\sum_{j=1}^{N} r_j^3}{R_\sigma^3}, \tag{12}$$

with N the number of monomers, each with radius r_j in an aggregate. For fluffy aggregates, ϕ_σ approaches 0, for compact aggregates it approaches 1. An illustration for a representative aggregate is shown in Figure 2. Even though this method is more complex, it provides a much more robust determination of the fluffiness of aggregates and is less expensive computationally.

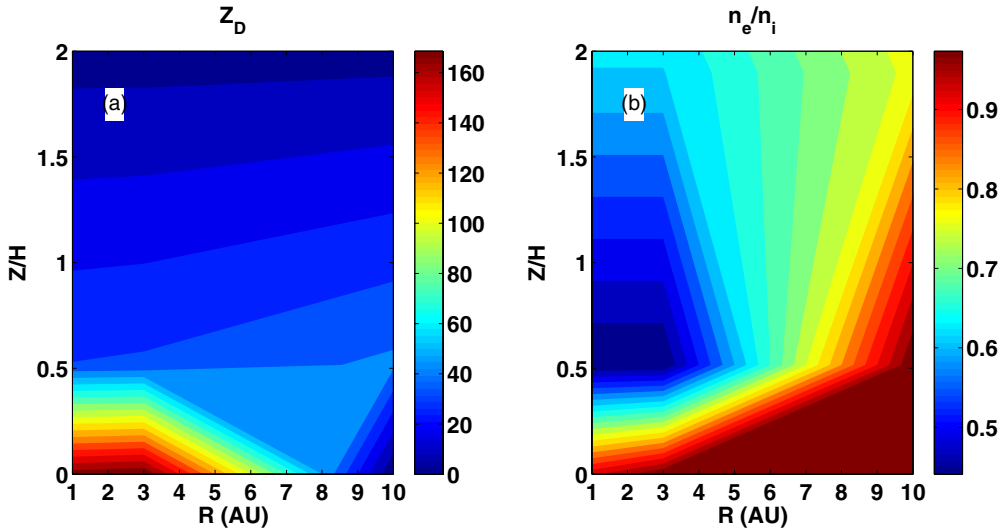

Figure 4. (a) The computed number of electrons on a 0.83 μm silicate particle, using the density, temperature, and fractional ionization profiles provided in Willacy et al. (1998) and Semenov et al. (2004). (b) The electron depletion effect, expressed as n_e/n_i for the same profiles as used in (a), with the assumption of a dust-to-gas mass density ratio of 1%.

(A color version of this figure is available in the online journal.)

3. INITIAL CONDITIONS FOR THE SIMULATIONS

3.1. Initial Monomer Distribution

In our simulations, the monomers are spherical particles with radii in the range $0.5\,\mu\text{m} < a_0 < 10\,\mu\text{m}$, distributed according to the Mathis–Rumpl–Nordsieck (MRN) distribution for dust grains in the interstellar medium (ISM), $n(a_0) \propto a_0^{-3.5} da_0$ (Mathis et al. 1977), which gives an average monomer radius of $\langle a_0 \rangle = 0.83\,\mu$m. Even though the sizes are larger than those in the MRN distribution for the ISM, the average monomer size is consistent with most assumptions for the "typical" grain size in PPDs and this larger size is usually ascribed to different mechanisms processing the smaller ISM particles into micrometer-sized particles which are then accreting in PPDs (Blum & Wurm 2008). Hence, the size distribution is also probably less steep, as shown for instance in Weidenschilling (1984).

For the monomer material we use silicate, which is commonly observed in primordial material in the solar system; specific absorption features for silicates are routinely observed in spectra from PPDs. The use of silicates should be especially relevant at the position in the disk considered here, but further out, beyond the snow-line, water ice particles will be abundant. Most importantly for our simulations, however, is that silicates are non-conducting particles, for which charge can be assumed to stick at the point of impact, exactly as our model assumes for aggregate charging.

3.2. Average Initial Monomer Charge and Electron Depletion Effect

In order to calculate the charge on an averaged-sized initial monomer, with $a = 0.83\,\mu$m, while taking the electron depletion effect into account, the plasma number density and temperature, and the dust number density need to be determined. In order to obtain the plasma density, the fractional ionization can be used, since the plasma density equals the fractional ionization times the neutral gas density. Due to the collisionality, the plasma will thermalize with the gas, so the neutral temperature can be used for the plasma temperature.

By combining the two-dimensional equilibrium fractional ionization profiles, presented in Figure 2 of Semenov et al. (2004), with the mid-plane neutral density and temperature profiles in Willacy et al. (1998), and by assuming a dust-to-gas mass density ratio of 1%, both Z_D and n_e/n_i can be calculated for the average silicate monomer with $a = 0.83\,\mu$m. The results are shown in Figure 4.

The plasma density and dust charge are the highest relatively close to the mid-plane, due to the fact that both the gas density and temperature are highest there. The electron depletion increases toward $Z/H \sim 0.5$, but then decreases again at larger values of Z/H, away from the mid-plane, due to the increased ionization rate from cosmic rays toward the upper edge of the PPD. The maximum obtained dust charge is about 170e, and it is interesting to note that the mid-plane dust charge remains fairly high as far out as 5 AU from the YSO, indicating that relatively high turbulent velocities are required for dust collisions all the way out to 5 AU. At 1 AU and at $Z/H \sim 0.5$ we have $Z_D \approx 60$ and $n_e/n_i \sim 0.5$. In order to investigate slightly different situations, in this paper we also include results for $n_e/n_i = 1$ and $n_e/n_i = 0.1$, as well as the neutral coagulation case.

3.3. Turbulent Velocities

We model the early solar system PPD, with a central YSO of 1 $M_\odot$, a mid-plane temperature of 1200 K and mass density of $\rho_g = 2 \times 10^{-9}$ g cm^{-3} (Ruden & Pollack 1991; Lissauer 1993). At 1 AU, we thus have $\Omega_K = 1.99 \times 10^{-7}$ s^{-1}, so that $t_L = 5.02 \times 10^6$ s. The local sound speed is defined as $c_g = \sqrt{\gamma k_B T/\mu \text{m}_H}$. With $\gamma = 7/2$, $\mu = 2.34$ and $T = 900$ K at $z = 0.5H$, we find $c_g = 2.11 \times 10^5$ cm s^{-1}. This way, the scale height becomes $H = c_g/\Omega_K = 0.071$ AU.

Choosing $\alpha = 0.01$, we find $V_L = 0.1 \times c_g = 2.11 \times 10^4$ cm s^{-1} and $L_L = 0.1 \times H = 0.0071$ AU. The molecular viscosity is calculated as $\nu_m(z) = \sqrt{2/\pi} m_g c_g/\rho_g \sigma_{\text{coll}}$ (Okuzumi et al. 2011b), which results in $\nu_m(0.5H) = 1.73 \times 10^5$ cm^2 s^{-1}. The Reynolds number then becomes $Re = \alpha c_g H/\nu_m = 1.3 \times 10^{10}$. The small eddy velocity, length and time-scale

are then found as $V_\eta = Re^{-1/4}V_L = 62.5$ cm s^{-1}, $L_\eta = Re^{-3/4}L_L = 2.75 \times 10^3$ cm, and $t_\eta = Re^{-1/2}t_L = 44.1$ s.

Since we require $t_{s,\max} < t_\eta$ for strongly coupled particles, the largest particles that would still be coupled for these conditions have radii of 12 cm, much bigger than our largest size of 10 μm. The maximum turbulent relative particle velocity between monomers will occur for a monomer of 10 μm radius and one of 0.5 μm radius, for which we find $(t_1 - t_2) \sim 5.7$ s. The maximum turbulent relative velocity becomes $v_{\rm turb,max} = \sqrt{3/2} * 62.5 * 5.7/44.1 = 9.9$ cm s^{-1}, just above $v_{r,\min}$.

This velocity is slightly below the restructuring threshold, but much lower than the velocity needed for destruction (Wurm & Blum 1998; Blum & Wurm 2000). In order for restructuring to play a significant role for the morphology of aggregates, the kinetic energy requirement is given by $K > 5E_{\rm roll}$, where $E_{\rm roll} = 6\pi^2\xi\gamma\alpha_\mu$ is the restructuring energy (Dominik & Tielens 1997). $\alpha_\mu = a_1a_2/(a_1+a_2)$ is the reduced radius for two monomers in contact during a collision, γ is the surface energy density for the material and $\xi_{\rm crit}$ is the critical displacement for a monomer in an aggregate after which restructuring starts. In Blum & Wurm (2000) γ was measured for pure silicate, SiO_2, as 0.019 J m^{-2}, while in Dominik & Tielens (1997) the value for *ices* was reported as 0.37 J m^{-2}, while $\xi_{\rm crit}$ was taken as 2 nm. For our example of the two monomers above, this results in a restructuring energy of $E_{\rm roll} = 6.7$ keV. Their kinetic energy is ~40 eV, however. Therefore, restructuring would become important when their relative velocity would be larger by a factor or roughly $\sqrt{167.5} \sim 13$, which gives a relative velocity threshold for restructuring on the order of 130 cm s^{-1}.

The real question of course is whether or not a collision between aggregates, or between monomers and aggregates can lead to restructuring. Since the kinetic energy depends quadratically on the velocity, the relative turbulent velocity will be the most important factor. The largest relative velocity occurs between the smallest monomer and the largest aggregate. The largest aggregate has $R \approx 100\,\mu$m with a mass of roughly $10^5 m_0 \approx 6.2 \times 10^{-7}$ g. Estimating the cross section $\sigma \approx \pi R^2 \approx 3.14 \times 10^{-4}$ cm^2, we find a stopping time of $t_{\rm agg} \approx 3.99$ s. The stopping time for the 0.5 μm monomer is 0.3 s. The relative turbulent velocity between the monomer and the aggregate then equals $v_{\rm turb} = 6.4$ cm s^{-1}, so that the kinetic energy becomes $K \sim 0.02$ keV. The restructuring energy is $E_{\rm roll} = 7$ keV, hence restructuring does not play a role. Apparently, larger size differences than obtained in the simulations presented here are required for restructuring to become important for aggregate morphologies in the considered PPD environments.

4. RESULTS

4.1. Aggregate Morphology

Figures 5(a), (b), and (c) show the maximum radius, R, for the largest aggregates formed in the different plasma environments, the mass in average monomer mass, m_0, and the equivalent radius, R_σ, respectively. The separate data points are shown for the case with $n_e/n_i = 1$. For all other data sets only the straight-line fits to the logarithmic data are shown.

It is clear that the more negatively charged the aggregates are, the larger they become and the more massive they become. The larger mass is also illustrated in Figure 6(a), where the size distribution of the monomers within the aggregates is shown. The higher the charge on the aggregates, the larger the contribution of monomers with larger radii becomes, while the smaller monomers become more underrepresented. This is due to the large relative velocities needed to overcome the Coulomb repulsion barrier, which requires a large size difference for the initial monomers. The monomers contained within the aggregates formed through neutral aggregation for the large part are distributed according to the initial monomer distribution within the PPD (the MRN distribution), as indicated by the dashed line.

Figure 6(b) shows the compactness factor for the aggregates. In this graph, all data points are also included for the neutral aggregates. This illustrates that the distribution in compactness factor is much broader than the distribution for the charged case. This trend is seen in all data; neutral aggregation allows a larger deviation from the mean values than charged aggregation, also for the mass and size of the aggregates. The results also show that higher aggregate charges lead to lower values for the compactness factor and hence fluffier, more porous aggregates.

This is also shown in Figures 7(a)–(d) where the compactness factor distribution is shown for the three aggregate generations for the different plasma environments. As the aggregates grow in size in later generations, the compactness factor shifts to lower values and becomes the lowest for the charged aggregates. The distribution is also slightly narrower for the charged aggregates, especially for the 2nd and 3rd generations.

Figures 7(e)–(h) show the same analysis for the fractal dimension. For later generations, the Hausdorff fractal dimension shifts to lower values, indicating a shift away from compact aggregates toward more linear structures. Due to the manner in which the fractal dimension is defined, the shift is much less pronounced than the shift in compactness factor, and the differences for the different plasma environments are not as clear.

4.2. Collision Statistics

The fact that charged aggregates are more porous might indicate that more aggregates are involved in successful collisions and less monomers are able to collide with the aggregates to fill in the open space. Figure 8 shows the contributions of both monomers and aggregates from earlier generations to the successful collisions; on the left for the formation of generation-2 aggregates, on the right for the formation of generation-3 aggregates. The bars labeled *Trgt* indicate the pre-set (target) percentages of the *incoming* aggregates and monomers, while the other bars indicate the actual monomer and aggregate contributions involved in successful collisions. The labels *q100*, *q50*, *q10*, and *Neut* refer to $n_e/n_i = 1.0$, $n_e/n_i = 0.5$, $n_e/n_i = 0.1$, and neutral aggregation, respectively.

In the case of neutral aggregation, the contribution to successful collisions of monomers and aggregates remains fairly close to the distribution of the incoming monomers and aggregates, even though the aggregates contribute slightly more to the formation of larger aggregates than the monomers do, but the deviation is 10% at most. In the case with the highest dust charge, for $n_e/n_i = 1.0$, the deviation from the incoming distribution is dramatic, with the contribution of aggregates 30% higher than the set percentage of incoming aggregates. This clearly shows that CCA is much more effective than PCA.

Figure 9(a) shows the average size of incoming aggregates in number of monomers versus the number of monomers in the resulting aggregate. It shows that aggregation occurs through the addition of smaller aggregates onto larger aggregates, since the resulting aggregate is up to 10× bigger than the incoming aggregate.

Figure 9(b) shows the average collision probability against the size of the target aggregate (the aggregate placed at the

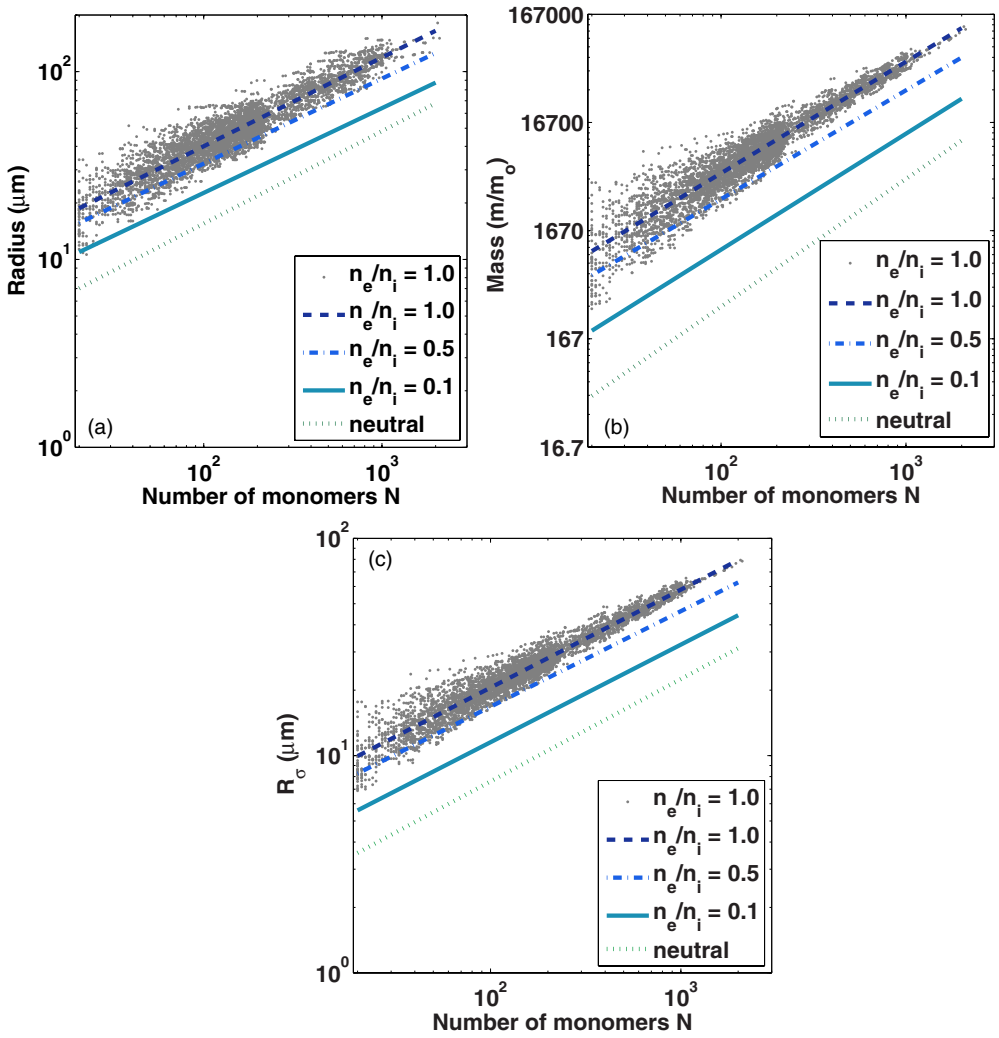

Figure 5. (a) The maximum radius of the aggregates against the number of monomers in the aggregates. (b) The aggregate mass in average monomer mass, m_0, against the number of monomers in the aggregates. (c) The equivalent radius, R_σ, in micrometer vs. the number of monomers in the aggregates.

(A color version of this figure is available in the online journal.)

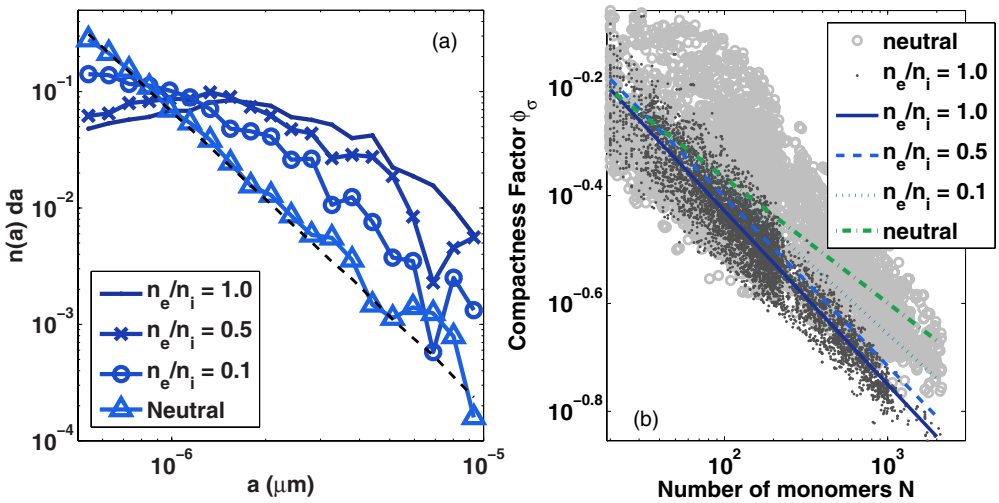

Figure 6. (a) The distribution of the monomers contained within the aggregates formed in the different plasma environments. The monomers within the neutral aggregates are distributed according to the initial monomer distribution in the disk, as indicated by the dashed line. (b) The compactness factor of the aggregates formed in the different plasma environments.

(A color version of this figure is available in the online journal.)

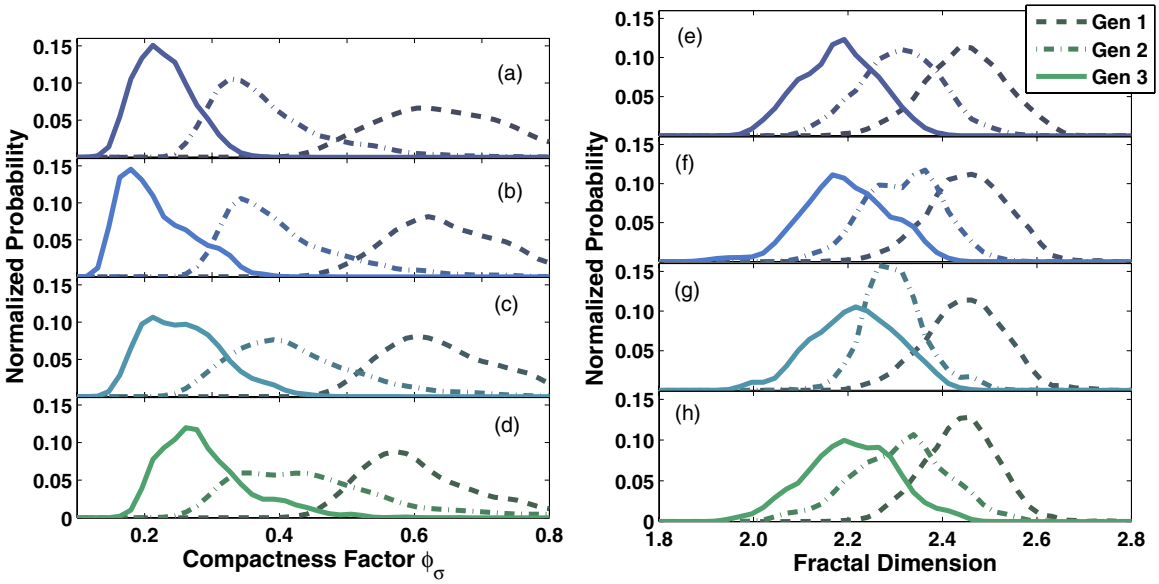

Figure 7. Compactness factor distributions for the case of $n_e/n_i = 1.0$ (a), $n_e/n_i = 0.5$ (b), $n_e/n_i = 0.1$ (c), and the neutral case (d), for the three aggregate generations, where the dashed lines indicate generation 1, dash-dotted lines indicate generation 2, and the solid lines indicate the generation 3. Panels (e)–(h) show the fractal dimension calculated using the box-counting or Hausdorff method.

(A color version of this figure is available in the online journal.)

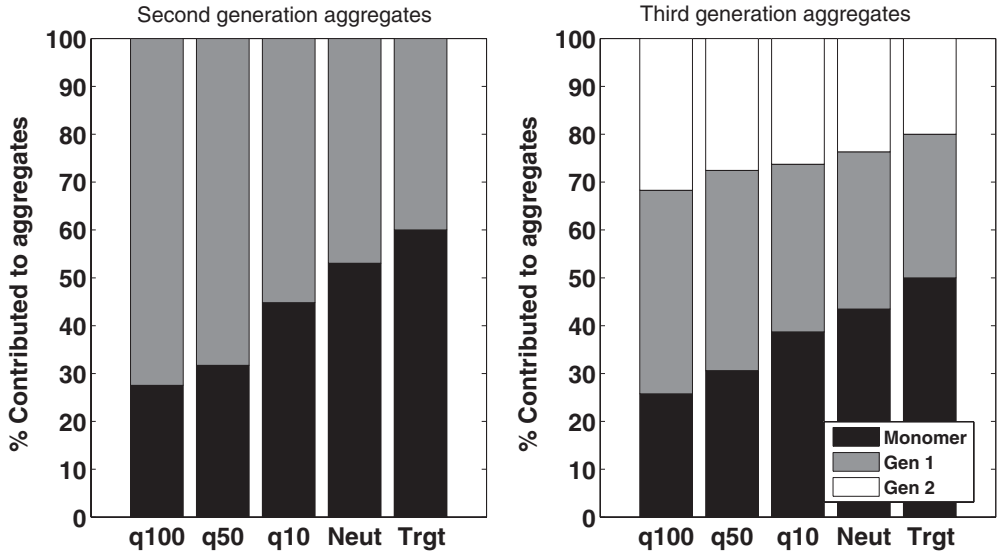

Figure 8. Contribution (in percent) of monomers and aggregates from the libraries to the successful collisions, for all aggregates formed in the second generation, on the left, and the third generation, on the right. *q100, q50, q10*, and *Neut* refer to the cases with $n_e/n_i = 1$, 0.5 and 0.1, and the neutral coagulation, respectively. *Trgt* refers to the percentages set in the model for the incoming particle type; 60% monomers, 40% first-generation aggregates for the second generation; 50% monomers, 30% first generation, and 20% second-generation aggregates for the third generation.

origin at which the incoming particle is "shot") in number of monomers. The collision probability is defined as the ratio of the number of successful collisions to the sum of the successful and missed collisions. For neutral aggregation, the collision probability does not vary much, between 100% for very small target aggregates and 60% for intermediate-sized aggregates. The probability for successful collisions for charged aggregates is much lower for small and large target aggregates. Very small aggregates are mostly built in the first generation, which involves particle–particle interactions. Due to the charge, a large size-difference between the monomers is required, which statistically has a small chance, so that many missed collisions will occur for every successful collision. Very large aggregates are made in the third generation and have the highest porosity. They therefore contain the largest amount of open space within their structure for incoming aggregates to move through without being successfully captured, while they also couple more effectively to the gas, and have lower relative velocities. The intermediate generation already include effective cluster–cluster aggregation, but are not yet so big as to contain too much open space.

4.3. Aggregate Charge and Dipole Moment

Although the charge and dipole moments play an important role in charged aggregate coagulation, their computation for larger aggregates quickly becomes computationally expensive. As such, for simulations of large aggregate populations, a heuristic fit for the charge and dipole moment based on some

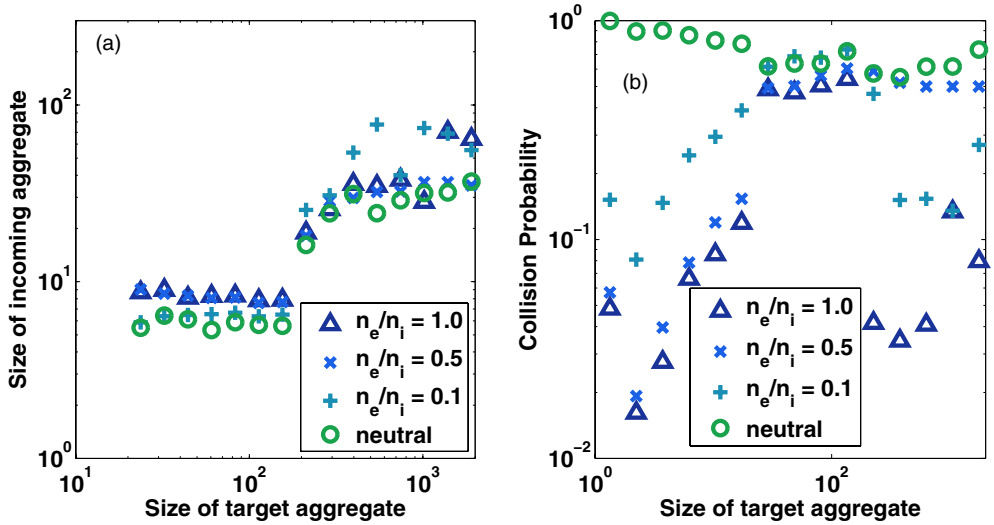

Figure 9. (a) Size of incoming aggregates in successful collisions against the size of the aggregate resulting from these collisions, in number of monomers. The data are averaged over many aggregate collisions. (b) The collision probability defined as the ratio of the number of successful collisions to the sum of the missed collisions and the successful collisions vs. the size of the target aggregate in number of monomers.

(A color version of this figure is available in the online journal.)

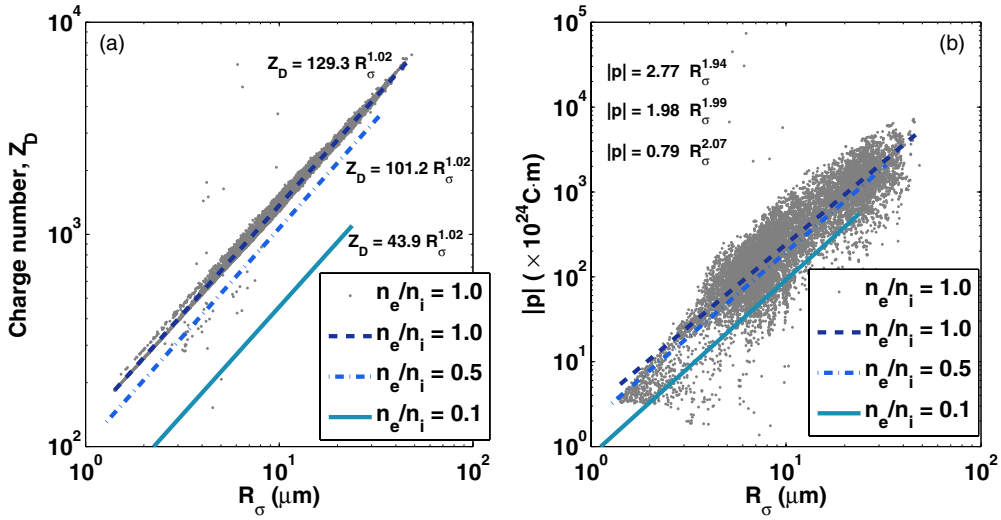

Figure 10. (a) The aggregate charge number, Z_D, vs. the equivalent radius, R_σ, in microns and (b) the aggregate dipole moment vs. equivalent radius. Note the log–log scale. The lines indicate linear fits to the log–log data. The aggregate charge depends linearly on the equivalent radius, whereas the dipole moment varies roughly with the square of the equivalent radius, hence with the orientation averaged projected surface area.

(A color version of this figure is available in the online journal.)

specific and easily measurable property of the aggregate would be valuable. Figure 10 shows the aggregate charge number, Z_D, and the aggregate dipole moment obtained from our simulations as a function of the equivalent radius, R_σ.

The charge on an aggregate is nearly linearly proportional to the equivalent radius for all environments, only the absolute value of the charge increases with decreasing electron depletion, as expected. Such a fit is useful when a complex *N*-body calculation of large populations is needed (Matthews & Hyde 2004), since then not all the aggregates have to be separately charged using OML_LOS, drastically decreasing the required computational time. A similar fit for the dipole moment has recently been published (Matthews & Hyde 2009) in terms of the number of monomers in the aggregate, albeit with a large amount of scatter. Using the equivalent radius, a good fit can be obtained from which the aggregate dipole moment is found to be proportional to the square of the equivalent radius. Similar to the charge, this heuristic fit can be used in large *N*-body simulations, rather than having to calculate it for every aggregate separately using OML_LOS.

5. DISCUSSION AND CONCLUSIONS

We have shown that the effect of charge on coagulation is very important for the formation of larger aggregates in PPDs and that significant aggregate charges are to be expected in a large part of the PPD. The main results can be summarized as follows.

1. Despite the electron depletion effect, significant negative charge on micron-sized silicate monomers ($Z_D > 50$) is possible in a large part of the PPD. Therefore, turbulent velocities seem to be a necessity for a large part of the PPD to allow for dust coagulation.

2. Coagulation of charged aggregates leads to more massive, larger, and fluffier aggregates than neutral aggregation, for the same number of monomers in the aggregate.
3. The electron depletion effect reduces the negative dust charge. The larger the effect, the more characteristics of the aggregates and coagulation approach the neutral case.
4. Charged aggregates contain a much larger fraction of larger, more massive monomers than neutral aggregates, which contain monomers distributed according to the initial distribution of the monomers in the disk.
5. In general, CCA is much more important than PCA, especially for charged coagulation.
6. Collision statistics indicate that neutral coagulation has the highest collision probability. In all plasma environments, aggregate growth occurs through the preferential incorporation of smaller aggregates, rather than monomers, into larger aggregates
7. A heuristic fit for the aggregate charge and dipole moment can be obtained in terms of the equivalent aggregate radius, R_σ. The dust charge is linearly proportional to R_σ, while the dipole moment is roughly proportional to R_σ^2.

5.1. Consequences for Planet Formation

An important observation is that dust charging is significant, at least up to radial distances of 5–7 AU from the YSO and a vertical distance of 0.5 H from the mid-plane, in an early solar system type PPD. This means that large relative particle velocities are required to allow micron-sized particles to collide and stick, which are most likely due to the occurrence of turbulence in the disk. In many models the presence of so called *dead-zones* toward the mid-plane, due to the optically thick character of the disk and hence the expected absence of a plasma-environment, would prevent disk-turbulence toward the mid-plane. However, the fractional ionization and temperature profiles employed here seem to allow for sufficient plasma for dust charging. Furthermore, recent simulations have shown that these dead-zones might be much smaller than previously anticipated (Turner et al. 2007).

From our simulations, we expect dust coagulation in the interior of the PPD, within ∼5 AU, to be dominated by charged coagulation. On the one hand, the collision probability seems to be significantly lower during the initial stage of aggregate formation (up to $N \sim 20$) and during the final stage of aggregate formation considered here (with $200 < N \sim 2000$). On the other hand, the sizes and masses of the formed charged aggregates are significantly larger for the same number of monomers in the aggregate, which would imply that the aggregates reach millimeter to centimeter sizes more rapidly, at which point they are believed to decouple from the gas. However, the latter effect only amounts to a factor of 3–5, while the difference in collision probability is up to two orders of magnitude.

Neutral aggregation is most likely dominant at radial distances greater than 10 AU, which is beyond the so called "snow-line," at which point water-ice particles become important. Even though neutral aggregates are smaller, the larger collision probability means that neutral aggregation will occur faster for the same initial monomer density. Depending on the dust density profile in the PPD, the growth time at 1 AU (dominated by charged aggregation) might be longer than at 10 AU (dominated by neutral aggregation), an observation also reported in Okuzumi et al. (2011b).

Another important observation is that charged aggregates predominantly contain the larger monomers from the initial monomer distribution, whereas monomers incorporated within neutral aggregates follow the initial monomer distribution. This means that in the inner regions of the PPD coagulation will deplete the dust of larger monomers, leaving a distribution of small monomers behind (assuming no replenishment of monomers occurs). Since large size differences between monomers then become unlikely, continued growth of small aggregates will be slowed down. Overall, this should significantly slow down the long-term coagulation of charged aggregates. A similar effect was reported in Okuzumi et al. (2011b), where a so-called *freeze-out* of small aggregates in regions with small ionization degree inhibited further aggregate growth as well.

5.2. Consequences for Observations

In situ measurements of dust particles are only possible within the solar system and have been performed using dust (counting) detectors on the *Ulysses* and *Galileo* missions (Grün et al. 1992), currently on the *New Horizons* mission on its journey to Pluto (Poppe et al. 2010), and of course by the collection of cometary dust in the *Stardust* and *Hayabusa* missions (Brownlee et al. 1997; Kawaguchi et al. 2008). Most dust detectors are limited to counting the number of events and the mass and charge (or their ratio). Dust return missions would allow the direct measurement of the morphology of the dust particles collected; however, the impacts of the particles occur at very high velocities and preventing the restructuring of the particles upon impact is a hard problem.

Overall, the number of impact events on each individual mission is limited and typically well below one hundred. This means that large population statistics is mostly unavailable. However, in the future, the cumulative distribution of masses, sizes, charges and porosities would provide a possible determination of the aggregation process and environment. For instance, neutral aggregation allows for much wider distributions in the masses and sizes than charged aggregation. Both this and the measured porosities could distinguish between aggregates formed through charged or neutral aggregation.

Fluffy aggregates will also have different optical properties than compact aggregates (Min et al. 2006), such as their scattering and extinction coefficients, so that the proper identification of aggregate distributions and their constituents, as well as the plasma environment in which they are immersed might well be derived from observations of the light originating from the dusty regions in observed PPDs, or by the light scattering and absorption properties of aggregates in the solar system, responsible for instance for the Zodiacal light. This could then provide a unique and direct measurement of solar system disk properties, such as the plasma densities and temperatures, at the earliest stages of planetary formation. The fact that charged aggregation results in depletion of the large monomers from the initial monomer distribution, while the size distribution is preserved in neutral aggregation, might be an additional way of determining the aggregation process and environment from optical observations of PPDs.

5.3. Consequences for Numerical Simulations

As mentioned in the introduction, the formation of the large gaseous planets in our solar system (and similarly for the ones observed around other stars) is typically assumed to take too long by the process of core-accretion (the accumulation of

small planetesimals, formed by dust accretion, into a rocky core massive enough to grow by its gravitational influence on the surrounding disk material), due to the low disk densities and temperatures. An alternative is the (gravitational) disk instability model, in which dense clumps grow through instabilities, which are consequently assumed to cool by radiation (Boss 1997, 2000).

An important question is the exact nature of the cooling mechanisms in the exterior regions of the PPD. In principle, the aggregates should play an important role in radiating away thermal energy from the disk, besides radiation by the gas itself. The efficiency of this process might strongly depend both on the material of the dust, but also on the fluffiness, since a large effective surface area would allow strong absorption of the energy from the gas via impinging molecules, as well as a large surface area for emitting (blackbody) radiation. The corresponding wavelength of the maximum intensity at which the aggregates would radiate, assuming that the aggregates reach thermal equilibrium with the gas at temperatures around 50 K, would be $\lambda_{\max} \sim 60\,\mu$m, according to Wien's displacement law. To be efficient radiators, the aggregate size has to be significantly bigger than this wavelength. In the simulations considered here, 60 μm is around the maximum size reached by the aggregates through neutral aggregation, whereas charged aggregation reaches sizes well over 100 μm. Therefore, the dust in the outer regions of PPD might not be very efficient radiators, unless more time is available for the aggregates to grow.

Finally, the increased surface area of fluffy aggregates will allow faster reaction rates for surface enhanced chemistry, believed to be important in PPDs, as shown by large-scale chemistry models of PPDs (Millar et al. 2003). Our results imply that less aggregate surface area is available from neutral aggregates, whereas charged aggregation leads to larger and more fluffy aggregates. The complex chemistry in PPDs might therefore be more effectively enhanced in the inner regions than in the outer regions, where the more compact aggregates reside.

This material is based upon work supported by the National Science Foundation under grant no. 0847127. Furthermore, authors are appreciative of the useful discussion with many of the CASPER members, as well as the helpful comments provided by the anonymous referee.

REFERENCES

Allen, J. E. 1992, Phys. Scr., 45, 497
Balbus, S. A., & Hawley, J. F. 1991, ApJ, 376, 214
Blum, J., & Wurm, G. 2000, Icarus, 143, 138
Blum, J., & Wurm, G. 2008, ARA&A, 46, 21
Blum, J., Wurm, G., Kempf, S., et al. 2000, Phys. Rev. Lett., 85, 2426
Boss, A. P. 1997, Science, 276, 1836
Boss, A. P. 2000, ApJ, 563, 367
Brauer, F., Dullemond, C. P., & Henning, Th. 2008, A&A, 480, 859
Brownlee, D. E., Tsou, P., Burnett, D., et al. 1997, Meteorit. Planet. Sci., 32, A22
Cuzzi, J. N., Hogan, R. C., Paque, J. M., & Dobrovolskis, A. R. 2001, ApJ, 546, 496
Dominik, C., & Tielens, A. G. G. M. 1997, ApJ, 480, 647
Dullemond, C. P., & Dominik, C. 2004, A&A, 421, 1075
Ehrenfreund, P., Fraser, H. J., Blum, J., et al. 2003, Planet. Space Sci., 51, 473
Grün, E., Baguhl, M., Fechtig, H., et al. 1992, Geophys. Res. Lett., 19, 1311
Hage, J. I., & Greenberg, J. M. 1990, ApJ, 361, 251
Kawaguchi, J., Fujiwara, A., & Uesugi, T. 2008, Acta Astron., 62, 639
Kempf, S., Pfalzner, S., & Henning, T. K. 1999, Icarus, 141, 388
Konopka, U., Mokler, F., Ivlev, A. V., et al. 2005, New J. Phys., 7, 227
Lissauer, J. J. 1993, ARA&A, 31, 129
Mathis, J. S., Rumpl, W., & Nordsieck, K. H. 1977, ApJ, 217, 425
Matthews, L. S., Hayes, R. L., Freed, M. S., & Hyde, T. W. 2007, IEEE Trans. Plasma Sci., 35, 260
Matthews, L. S., & Hyde, T. W. 2003, J. Phys. A: Math. Gen., 36, 6207
Matthews, L. S., & Hyde, T. W. 2004, IEEE Trans. Plasma Sci., 32, 586
Matthews, L. S., & Hyde, T. W. 2009, New J. Phys., 11, 063030
Mendis, D. A., & Rosenberg, M. 1994, ARA&A, 32, 419
Millar, T. J., Nomura, H., & Markwick, A. J. 2003, Ap&SS, 285, 761
Min, M., Dominik, C., Hovenier, J. W., de Koter, A., & Waters, L. B. F. M. 2006, A&A, 445, 1005
Nakamura, R., & Hidaka, Y. 1998, A&A, 340, 329
Nübold, H., Poppe, T., Dominik, C., & Glassmeier, K.-H. 2002, Adv. Space Res., 29, 773
Okuzumi, S. 2009, ApJ, 698, 1122
Okuzumi, S., Tanaka, H., Takeuchi, T., & Sakagami, M. 2011a, ApJ, 731, 95
Okuzumi, S., Tanaka, H., Takeuchi, T., & Sakagami, M. 2011b, ApJ, 731, 96
Ollivier, M., Encrenaz, T., Roques, F., Selsis, F., & Casoli, F. 2009, Planetary Systems. Detection, Formation and Habitability of Extrasolar Planets (Berlin: Springer)
Ormel, C. W., & Cuzzi, J. N. 2007, A&A, 466, 413
Perry, J. D., Matthews, L. S., & Hyde, T. W. 2010, IEEE Trans. Plasma Sci., 38, 792
Pollack, J. B. 1984, ARA&A, 22, 389
Poppe, A., James, D., Jacobsmeyer, B., & Horányi, M. 2010, Geophys. Res. Lett., 37, L11101
Qiao, K., Benesh, M., & Hyde, T. 2007, IEEE Trans. Plasma Sci., 35, 346
Raymond, S. N., Mandell, A. M., & Sigurdsson, S. 2006, Science, 313, 1413
Rice, W. K. M., Lodato, G., Pringle, J. E., Armitage, P. J., & Bonnell, I. A. 2004, MNRAS, 355, 543
Richardson, D. C. 1993, Icarus, 115, 320
Ruden, S. P., & Pollack, J. B. 1991, ApJ, 375, 740
Semenov, D., Wiebe, D., & Henning, Th. 2004, A&A, 417, 93
Shakura, N. I., & Sunyaev, R. A. 1973, A&A, 24, 337
Smith, B. A., & Terrile, R. J. 1984, Science, 226, 1421
Spitzer, L., Jr. 1941, ApJ, 93, 369
Turner, N. J., Sano, T., & Dziourkevitch, N. 2007, ApJ, 659, 729
Vasut, J. A., & Hyde, T. W. 2001, IEEE Trans. Plasma Sci., 29, 231
Velikhov, E. P. 1959, Sov. Phys. JETP, 36, 995
Weidenschilling, S. J. 1984, Icarus, 60, 553
Whipple, E. C., Jr., Northrop, T. G., & Mendis, D. A. 1985, J. Geophys. Res., 90, 7405
Willacy, K., Klahr, H. H., Millar, T. J., & Henning, Th. 1998, A&A, 338, 995
Wurm, G., & Blum, J. 1998, Icarus, 132, 125
Zsom, A., Sándor, Zs., & Dullemond, C. P. 2011, A&A, 527, A10